Supplementary Materials for

Interfacial instability for droplet formation in two-layer immiscible liquids under rotational oscillation

Linfeng Piao[1] and Hyungmin Park[1,2*]

[1]Department of Mechanical Engineering, Seoul National University, Seoul 08826, Korea

[2]Institute of Advanced Machines and Design, Seoul National University, Seoul 08826, Korea

List of movies

Movie S1. Oscillating wave patterns developing on an interface between two superposed immiscible liquids (silicone oil of 100 mm^2/s in upper layer and DI water in lower layer) along the periphery (near-wall region) of the azimuthally oscillating cylindrical container. The typical angular amplitude and frequency are $\Phi_o = 180°$ and f_ω =1.2 Hz, respectively. The movie plays 4 times slower than the real time.

Movie S2. Single water droplet forming on the interface between two superposed immiscible liquids (silicone oil of 100 mm^2/s in upper layer and DI water in lower layer) at the core (center) region of the cylindrical container during rotational oscillation. This droplet bounces off according to the periodic up-downs of the interface while staying above the center area. The typical angular amplitude and frequency are $\Phi_o = 175°$ and $f_\omega = 1.44$ Hz, respectively. The movie plays 4 times slower than the real time.

Movie S3. Multiple water droplets breaking off from the wavy interface between two superposed immiscible liquids (silicone oil of 100 mm^2/s in upper layer and DI water in lower layer) at the near-wall region of the cylindrical container during rotational oscillation. It will take some time for the appearance of multiple-droplet. The typical angular amplitude and frequency are $\Phi_o = 160°$ and $f_\omega = 2.30$ Hz, respectively. The movie plays in the real time.

Movie S4. Emulsion droplets (oil-in-water) forming in two superposed immiscible liquids (silicone oil of 100 mm^2/s in upper layer and DI water in lower layer) in the azimuthally oscillating cylindrical container. The population of the oil droplets in water formed at the near-wall region increase explosively at $t^* > 5.0$ ($t^* = t\omega/2\pi$). The typical angular amplitude and frequency are $\Phi_o = 175°$ and $f_\omega = 2.26$ Hz, respectively. The movie plays The movie plays in the real time.

Verification on effect of capillary waves originated from a meniscus on interfacial dynamics

To avoid the distortions of the contact line at the container wall, which may influence the observed instabilities in the present study, we have treated the inner wall surface of the containers by plasma before each run of the experiment. This leads to a meniscus (curved oil-water interface) formed at the wall when the oil and water are stably superposed in the container. As the alternative upward-downward motion of the oil-water interface is induced during the oscillation, the capillary waves may be emanated from such the meniscus geometry (Shao et al. 2021). Here, we intentionally change the meniscus geometry to discuss the effect of resulting capillary waves on the interfacial dynamics. As shown in figure S1, we first define the height of meniscus, i.e., distance between the contact line and liquid front ($\Delta_{m,i}$). When the cylindrical container is first filled with deionized (DI) water (H = 50 mm) and then the silicone oil is slowly added up to the same height, which results in the meniscus geometry like $\Delta_{m,3}$. As the contamination on the wall increases due to the repeated experiments, meniscus height is reduced to $\Delta_{m,2}$ and $\Delta_{m,1}$. Despite this is an undesired phenomenon in experiments, herein, we use it to control the meniscus geometry. It is noted that in order to obtain the reliable (consistent) results, we stopped the experiments and re-prepared fluid layers before the meniscus changes.

Now, we plot the critical frequency for the onset of interfacial waves and single-droplet formation at a given angular amplitude (figure S1). Here, it is noted that $\Delta_{m,1}$ represents the flat interface (without a meniscus) and $\Delta_{m,3}$ is the case we tested in the present study. As shown, the critical frequency for interfacial waves only increases about 6% when Δ_m increases about 300% (relative to $\Delta_{m,1}$). The critical frequency for SD formation varied about 3.8%. Considering the negligible errors caused by the minor distortion of the contact line (Talib et al. 2007; Jalikop & Juel 2009), together with this quantification, we believe that the capillary wave emanated from the wall, if any, would not be significant in the present setup. In addition, we find that despite the existence of a meniscus ($\Delta_{m,3}$), the axial rise height shows the same trend as the case of a flat interface ($\Delta_{m,1}$); its difference is only 0.8% (figure S2).

On the other hand, according to Shao et al. (2021), the amplitude of the capillary wave is usually much smaller than that at the resonant condition. Thus, it is inferred that the effect of the capillary waves would be very weak when the driving frequency is far from the critical frequency for parametric excitation. For a capillary wave, the dispersion relation is scaled as $\omega^2 = C\,\sigma/\rho\,(k)^3$ (Puthenveettil & Hopfinger 2009). Here, ω is the angular wave frequency and k is the wavenumber. Meanwhile, the waves with the largest amplitude is excited at $\omega = \omega_o/2$, where ω_o is the forcing frequency (Goodridge et al. 1997). With $k^{-1} \sim \Delta_m \simeq R\tan\theta = 4\times10^{-3}$m (where the angle at the wall θ = 6.6º and R = 35 mm reported by Shao et al. (2021)), the resonant driving frequency of the capillary wave of their system can be estimated as about 10.7 Hz (C = 1.0), similar to their experimental result of 11.20 Hz. Based on the same scaling analysis, the critical driving frequency for our system is estimated to be 16.1 Hz (corresponding to $k^{-1} \sim 2\times10^{-3}$ m) that is much higher than the frequency range of 0.1-3.5 Hz we have tested. Therefore, this also supports our reasoning that the effect of capillary waves, originated from the boundary, would be insignificant.

Contribution distinction for destabilization of interfacial waves based on energy analysis

According to the previous studies (Hooper & Boyd 1983; Hu & Joseph 1989; Boomkamp & Miesen 1996), the energy budget analysis can be used to distinguish the energies primarily supplied for inducing wave instability. For the classical Kelvin-Helmholtz (K-H) instability of inviscid fluids, Boomkamp & Miesen (1996) reported that the Reynolds stress in the vortex sheet will be the energy source of such an instability. When the density contrast (0.968 for the current study) is approximated as about 1.0, the rate of energy transfer from the mean flow to the disturbance *via* Reynolds stress is then expressed as $REY_j = (1/\lambda)\iint[-u_j v_j (dU_j/dy)]_{y=0}\,dxdy$ and the rate of the work done by the interface in the tangential direction is written as $\mathrm{TAN} = (1/\lambda)\int[(u_2-u_1)T_j^{xy}]_{y=0}\,dx$, where $T_j^{xy} = \nu_j(\partial u_j/\partial y + \partial v_j/\partial x)$ and subscript ‘j’ is 1 or 2 representing the upper and lower layers, respectively. In the present study, we assume that the velocity scale is u for the disturbed flow and $U = R\omega$ (azimuthal velocity) for the undisturbed (base) flow (Yoshikawa & Wesfreid 2011a), respectively. The characteristic length is the Stokes boundary layer thickness ($\delta_2 = \sqrt{2\nu_2/\omega}$) in lower layer (Yoshikawa & Wesfreid 2011a). In the azimuthal direction, the base flow U_2 in the lower (i.e., water) layer is nearly 0 compared to U_1 (the maximum U_1 is equivalent to U) in the upper layer (Yoshikawa & Wesfreid 2011b). Thus, REY (= REY_1) can be scaled as $u^2(R\omega/\delta_2)$ and TAN is scaled as $u^2(\nu_1/\delta_2^2)$. The competition between these can be expressed as TAN/REY = $\nu_1/(R\omega\delta_2)$, implying that the dominant component for the instability depends on the frequency (ω) and viscosity contrast (Yoshikawa & Wesfreid 2011a). Here, TAN/REY$\gg$1 means that the velocity-induced mechanism is dominant, otherwise the K-H type instability becomes dominant.

Set-up for PIV measurement and procedures

Here, to support our analysis results, we measure the velocity in the oil layer induced by the rotational oscillation using a high-speed particle image velocimetry (PIV) (figure S3a). The high-speed camera is used to capture images (with a resolution of 980 x 890 pixels) at 1200 Hz in the r-θ plane, but to acquire images (820 x 400 pixels) at 800 Hz in the r-z plane. As shown in figure S3(b) and (c), the field-of-view (FOV) to measure is illuminated by a green laser sheet (532 mm wavelength) from a continuous-wave laser (RayPower 5000, Dantec Dynamics). As the tracking particles, the hollow glass spheres with a diameter of 10 μm are used in the oil layer. The optical effect associated with the curvature of the sidewall of the cylindrical container was compensated for by calibrating the whole area of FOV in the plane of focus with a grid (a gap of grids is 0.02R) distortion test target (figure S3b). The velocity vectors with a 32 x 32 pixels interrogation window are then evaluated by the cross-correlation based on Fourier transforms. The 50% overlap of interrogation windows produces a spatial resolution of nearly 0.02R.

Oscillatory azimuthal velocity and stokes boundary layer in the oil layer

As reported in the main text, the interfacial wave developed in the near-wall region is found during the rotational oscillation. However, different from the frozen wave formed through the short wave instability of steady two-layer Couette flows reported by Yoshikawa & Wesfreid (2011b), the observed wave patterns oscillate with the driving frequency due to the relative oscillatory motion between oil and water layers. In general, since there is a considerably thin boundary layer in water ($\delta_w/R \ll 1.0$), this relative motion results from the contribution of the oscillatory azimuthal velocity in the oil layer, rather than in the water layer (Shyh & Munson 1986; Yoshikawa & Wesfreid 2011b). Thus, we plot the temporal variation of dimensionless azimuthal velocity ($u_\theta/A\omega$) at a given r/R = 0.8 (near-wall region) for the case of f_ω = 1.0 Hz and Φ_o=180°, as shown in figure S4(a). The positive velocity means that the azimuthal velocity in the oil layer is counterclockwise. It is clear that the azimuthal velocity in the oil layer exhibits oscillatory behaviors with time. This supports the fact that the formed wave patterns look oscillatory rather than stationary in the rotationally oscillating cylindrical container. Moreover, at a fixed time t^* = 0.625, the variation of azimuthal velocity with radial direction (r/R) is shown in figure S4(b). Considering the accuracy of measures in the blurred region, we measure the velocity within r/R = 0.9. Here, the velocity increases with r in a certain region ($1\text{-}\delta^* < r/R <$ 1.0 where $\delta^* = 4.6\delta_o/R$) and approaches the sidewall velocity. We find that this region, i.e., Stokes boundary layer, is similar to that theoretically derived in the literature (Schlichting & Gersten 2016), which denotes the position of $u_\theta/A\omega \approx 0.01$. It is worth to mention that the various symbols represent the different positions (i.e., laser sheet) of the measurements, and the azimuthal velocities measured at different positions show the same trend and overlap each other. Thus, this indicates that the velocity profile in Stokes boundary layer induced by the oscillating sidewall is uniform in the z-direction (Yoshikawa & Wesfreid 2011b).

Interaction between oil-water interface and surrounding velocity field in the oil layer

In order to understand the formation of the single-droplet (SD) associated with dynamics of the oil-water interface at the core region, we investigate the interaction between the interface and surrounding fluid (oil) based on the PIV measurement results in r-z plane. As shown in figure S5, for example, the in-plane velocity field and azimuthal vorticity (ω_θ) contour for the case of f_ω =1.6 Hz and Φ_o=180° are presented side-to-side with the corresponding raw image. This typical picture exhibits the instantaneous downward motion of the interface. It is found that the azimuthal vortex structure (highlighted by an arrow) forms locally near the interface during downward motion. This causes the acceleration of the surrounding oil in both radial and vertical directions near the interface (figure S5). This inertial effect might again act on the interface and induce the non-uniform vertical/radial deformation of interface along the radial direction, resulting in the formation of the high inclination angle (curvature at the axial line) of the interface. To support this, we provide the flow fields at the different angular amplitudes (Φ_o = 150°, 165° and 180°) with the fixed f_ω =1.4 Hz (figure S6). Among these, the SD only forms at Φ_o = 180° (figure S6c) and the streamlines are drawn additionally to assist to understand the flow in the plane. For analysis, two instantaneous events: t^* = 1.2 when the interface approaches the maximum rise h_1 at the first cycle and t^* = 1.4 where the interface moves downward are selected. We find that there exist local vortex structures near the interface (z < 0.1H) when approaching h_1 (t^* = 1.2) and the vorticity strength increases with Φ_o. With the downward movement of the interface profile, vortex structures are accompanying near the whole interface. However, the contrast of the vorticity strength between r = 0.1R (near axial line) and r = 0.2R is more considerable for the case of Φ_o=180° than cases of Φ_o = 150° and 165° (see t^* =1.4 in figure S6). As a result, the inclination angle of the observed interface is the highest at Φ_o = 180°, finally leading to the formation of the SD. Therefore, the interaction between the interface and surround fluid especially including vortex-induced hydrodynamic forces (e.g., inertial force exerted by fluid displacement) is also as important as the centrifugal force (due to the rotational motion of the oil in the upper layer) and gravitational force when determining the characteristics of the interface (e.g., inclination angle and curvature) as we discussed in the main text.

References

Boomkamp, P. A. M. & Miesen, R. H. M. 1996 Classification of instabilities in parallel two-phase flow. *Int. J. Multiph. Flow* 22, 67-88.

Goodridge, C. L., Shi, W. T., Hentschel, H. G. E., & Lathrop, D. P. 1997 Viscous effects in droplet-ejecting capillary waves. *Phys. Rev. E 56*, 472.

Hooper, A. P. & Boyd, W. G. C. 1983 Shear-flow instability at the interface between two viscous fluids. *J. Fluid Mech.* 128, 507-528.

Hu, H. H. & Joseph, D. D. 1989 Lubricated pipelining: stability of core annular flow. Part 2. *J. Fluid Mech.* 205, 359-396.

Jalikop, S. V., & Juel, A. 2009 Steep capillary-gravity waves in oscillatory shear-driven flows. *J. Fluid Mech.* 640, 131-150.

Puthenveettil, B. A., & Hopfinger, E. J. 2009 Evolution and breaking of parametrically forced capillary waves in a circular cylinder. *J. Fluid Mech.* 633, 355-379.

Schlichting, H., & Gersten, K. 2016 *Boundary-layer theory*. Springer.

Shao, X., Gabbard, C. T., Bostwick, J. B., & Saylor, J. R. 2021 On the role of meniscus geometry in capillary wave generation. *Exp. Fluids 62*, 1-4.

Shyh, C. K., & Munson, B. R. 1986 Interfacial instability of an oscillating shear layer. *ASME J. Fluids Eng.* 108, 89–92.

Talib, E., Jalikop, S. V., & Juel, A. 2007 The influence of viscosity on the frozen wave instability: theory and experiment. *J. Fluid Mech.* 584, 45-68.

Yoshikawa, H. N., & Wesfreid, J. E. 2011a Oscillatory Kelvin–Helmholtz instability. Part 1. A viscous theory. *J. Fluid Mech.* 675, 223-248.

Yoshikawa, H. N., & Wesfreid, J. E. 2011b. Oscillatory Kelvin–Helmholtz instability. Part 2. An experiment in fluids with a large viscosity contrast. *J. Fluid Mech.* 675, 249-267.

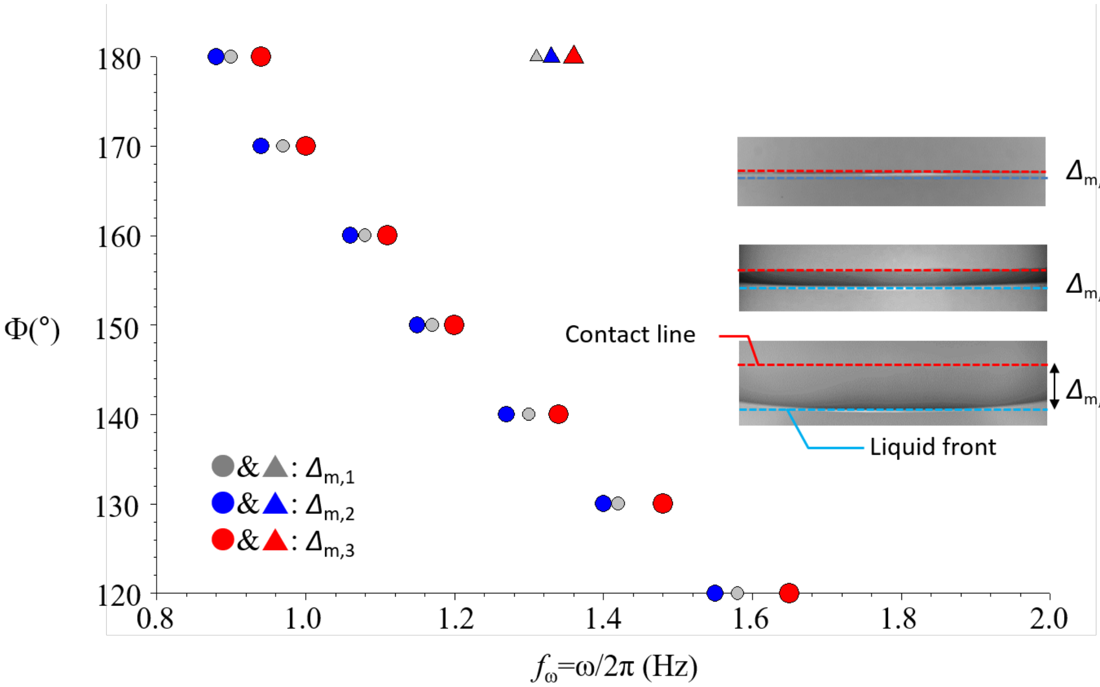

Figure S1. Variation of the critical frequency for onset of instability (circles, interfacial wave; triangles, SD formation) at the given angular amplitude, with $\Delta_{m,i}$.

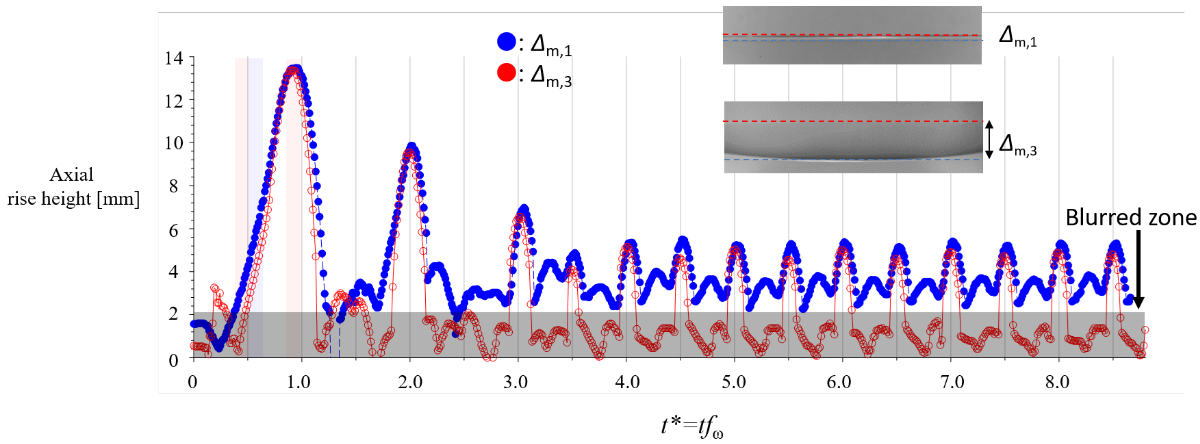

Figure S2. Variation of the axial rise height with dimensionless time ($t^*=tf_\omega$), comparing the cases of $\Delta_{m,1}$ and $\Delta_{m,3}$, for Φ =180° and f_ω = 0.94 Hz.

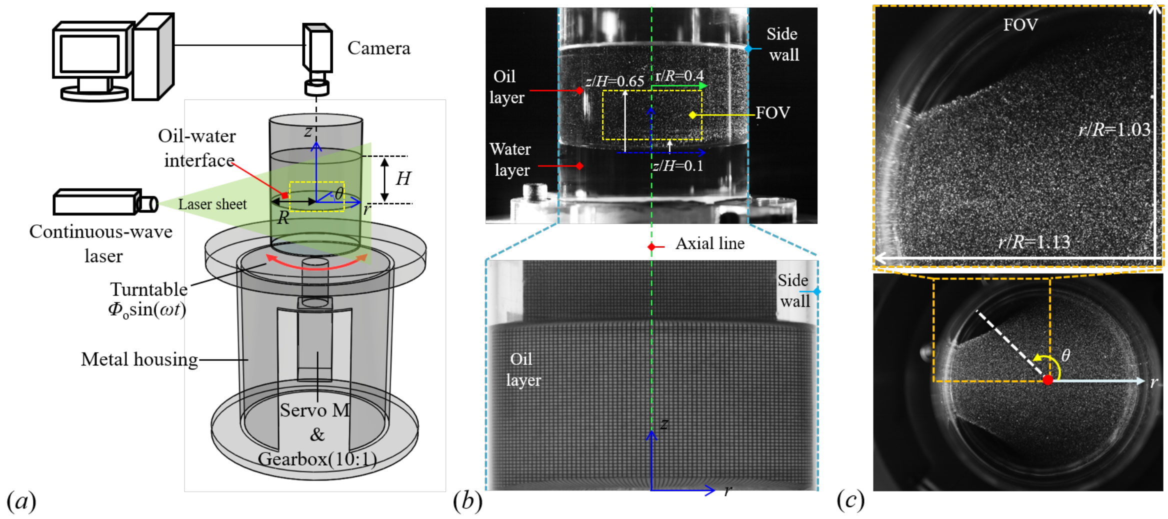

Figure S3. (*a*) Schematic diagram of the experimental set-up for high-speed particle image velocimetry (PIV) in the oil layer. (*b*) Raw image measured at side planes (r-z) with 1.0R x 0.65H field of view (FOV). The inset at below provides optical distortion correction by a grid distortion test target, of which gap is 0.02R. (*c*) Raw image visualized from the top planes (r-θ). The area of FOV in the plane of focus with 1.13R x 1.03R is highlighted right above the raw image.

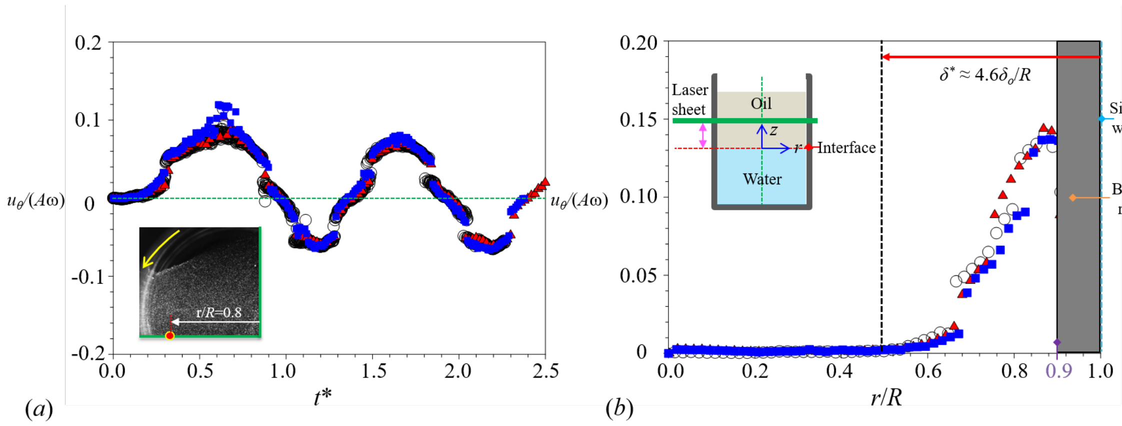

Figure S4. (*a*) Dimensionless azimuthal velocity by forcing velocity ($A\omega$) versus dimensionless time ($t^* = t\omega/2\pi$) at r/R=0.8 (marked by red closed circle). (*b*) Variation of azimuthal velocity with radial direction (r/R) at t^* = 0.625. Here, the frequency and angular amplitude of the rotational oscillation are f_ω = 1.0 Hz and Φ_o =180°, respectively. The symbols represents the different positions (i.e., laser sheet position) of measurements: ○, z/H=0.4; ▲, z/H=0.2; ■ z/H=0.1.

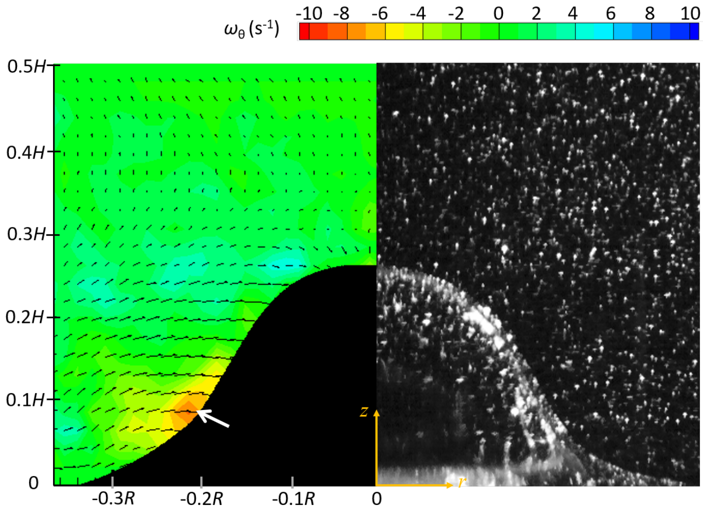

Figure S5. Typical in-plane velocity field and azimuthal vorticity (ω_θ) contour near the oil-water interface at $t^* = 1.48$ (downward motion) for the case of $f_\omega = 1.6$ Hz and $\Phi_o = 180°$. Here, the raw image is located side-to-side for the comparison.

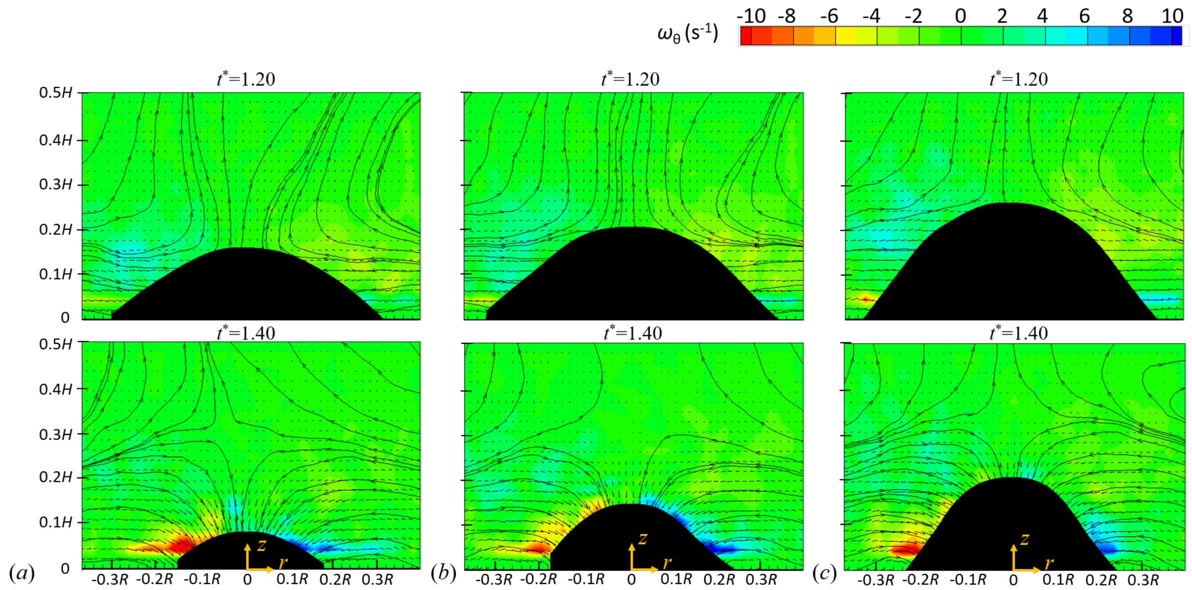

Figure S6. In-plane velocity field and azimuthal vorticity (ω_θ) contour near the oil-water interface at $t^* = 1.20$ (approaching maximum rise h_1) and $t^* = 1.40$ (downward motion) for different angular amplitude: (*a*) $\Phi_o = 150°$; (*b*) 165°; (*c*) 180°(SD) and $f_\omega = 1.4$ Hz.